Journal of Alloys and Compounds 1005 (2024) 175861

Contents lists available at ScienceDirect

Journal of Alloys and Compounds

journal homepage: www.elsevier.com/locate/jalcom

# Hyaluronic acid mediated ZnO-NPs: In relation to electrical and photocatalytic activity for dye degradation

Abdullah Akkaya [a,*], Ebru Karakaş Sarıkaya [b], Osman Kahveci [c], Raşit Aydın [d], Bünyamin Şahin [b,e], Enise Ayyıldız [c,f]

[a] Mucur Technical Vocational Schools, Tech. Prog. Department, Kırşehir Ahi Evran University, Kırşehir, Turkey
[b] Department of Basic Sciences, Faculty of Engineering, Necmettin Erbakan University, Konya, Turkey
[c] Department of Physics, Faculty of Sciences, Erciyes University, Kayseri, Turkey
[d] Department of Physics, Faculty of Sciences, Selçuk University, Konya, Turkey
[e] BITAM-Science and Technology Research and Application Center, Necmettin Erbakan University, Konya, Turkey
[f] Energy Conversation Research and Application Center, Erciyes University, Kayseri, Turkey

ARTICLE INFO

*Keywords:*
ZnO
Hyaluronic acid
TLM method
Resistivity
Photocatalytic activity

ABSTRACT

Various processes have been implemented to purify water; however, photocatalysis is comprehensively utilized in wastewater treatment and plays a significant role in water remediation. A photocatalyst is a nanostructured metal oxide ZnO nanoparticles, which boosts the reaction rate by its existence. ZnO nanoparticles show great performance in the absorption of various organic pollutants from wastewater. The objective of this research was to enhance the photocatalytic degradation performance of HA-added ZnO NPs using methylene blue as a model wastewater. Adjusting the main physical properties and photocatalytic efficiency of ZnO-NPs was performed using hyaluronic acid (HA), a natural bioactive stabilizer. The characterization of the fabricated ZnO-NPs samples with and without HA involved the utilization of FE-SEM, AFM, XRD, FTIR, PL, and I-V. As demonstrated by the FE-SEM analysis, ZnO formed rod-like structures, 3.0 % HA:ZnO exhibited cauliflower-like structures, and 5.0 % HA:ZnO displayed honeycomb-like structures. The X-ray diffraction (XRD) analysis demonstrated that the HA:ZnO nanoparticles exhibited hexagonal wurtzite structures. The average crystallite sizes of the ZnO, 3.0 % HA:ZnO, and 5.0 % HA:ZnO NPs were determined to be 25.20, 27.30, and 20.20 nm, respectively, using the XRD patterns. The surface area was 4.439, 2.987, and 5.204 $m^2/g$ of bare ZnO, 3.0 % HA:ZnO, and 5.0 % HA:ZnO-NPs were 4.439, 2.987, and 5.204 $m^2/g$, respectively. It is very likely that there are two different decay and/or capture mechanisms in the emission spectra because the TRPL decay profile behaves in a double-exponential way. The fast decay time constant ($\tau_1$) was 212 ps for bare ZnO and 3.0 % HA:ZnO NPs and 231 ps for 5.0 % HA:ZnO NPs. The slow decay time constant ($\tau_2$) has a similar pattern, with values of 3.716, 2.836, and 2.984 ns. The specific contact resistance values of the ZnO NPs increased from 0.113 to 45.624 ( $\times 10^5$ $\Omega$ $cm^2$) as a function of the HA concentration, as evidenced by the results of the electrical studies. The outcomes of this research present comprehensive information on noble-modified ZnO-NP materials containing HA for direct applications in electronic materials and photocatalytic degradation of organic waste in water.

## 1. Introduction

Metal oxides (MO) such as Iron Oxide ($Fe_2O_3$), Aluminum Oxide ($Al_2O_3$), Zinc Oxide (ZnO), Silicon Dioxide ($SiO_2$), Copper Oxide (CuO), Magnesium Oxide (MgO), and Nickel Oxide (NiO) are versatile materials with properties that can be tailored for a variety of applications through careful control of their composition, structure, and morphology. These materials have been extensively studied by researchers because of their diverse properties and wide range of applications in various fields, including optics, energy storage, electronics, environmental protection, and catalysis [1–7].

Among the various MOs, ZnO is a highly versatile material with a wide range of applications due to its distinctive properties. ZnO is an oxide semiconductor belonging to the II-VI group with a bandgap of approximately 3.37 eV at room temperature. The wide bandgap of ZnO makes it a promising material for various applications, including

* Corresponding author.
*E-mail address:* abdullah.akkaya@ahievran.edu.tr (A. Akkaya).

https://doi.org/10.1016/j.jallcom.2024.175861
Received 18 June 2024; Received in revised form 29 July 2024; Accepted 3 August 2024
Available online 5 August 2024

optoelectronic devices, UV lasers, and photocatalysts. It is an n-type semiconductor because of the presence of oxygen vacancies and zinc interstitials. The unique properties such as high exciton binding energy (60 meV) make it suitable for various applications in electronics, optics, and catalysis [8–12].

ZnO can be produced using various techniques such as chemical vapor deposition, sol-gel, spray pyrolysis, hydrothermal synthesis, precipitation method, combustion synthesis, mechanical milling, electrodeposition, and successive ionic layer adsorption and reaction (SILAR), each offering different advantages and special properties [13–17]. Among the above methods, SILAR offers significant advantages such as controlled thickness and uniformity, low-temperature processing, cost-effectiveness, versatility and flexibility, environmental friendliness, and high purity and quality of films and nanostructures [18–20].

Enhancing the physical properties and morphology of ZnO films is of paramount importance for optimizing their performance in a multitude of applications. A number of techniques can be employed to achieve these improvements, including doping with elements, the use of surfactants, post-deposition annealing, optimizing synthesis conditions, and the use of advanced deposition techniques [21–24]. D-glucuronic acid and N-acetyl-D-glucosamine repetitions joined by glycosidic bonds to form an anionic, non-sulfated, hydrophilic glycosaminoglycan structure make up hyaluronic acid (HA), a copolymer. HA, a non-toxic, water-soluble, biocompatible compound, is a macromolecule used in biomedical applications due to its viscous properties, hydrodynamic properties, and water retention capacity [25–27]. Since technology has advanced so quickly in recent years, a large number of organic chemicals that are utilized in various sectors and released into the environment have the potential to be extremely harmful to humans due to their toxicity and carcinogenicity. In particular, the textile industry's effluent is contaminated with dangerous organic pollutants like dyes, which are extremely poisonous, non-biodegradable, and bad for the environment and human health. Consequently, it is critical to rid natural waterways and wastewater of these organic contaminants [28,29]. Utilizing photocatalysts is one of the chemical methods for breaking down organic pollutants; its effective degradation and promising characteristics have drawn attention. The perfect way to exploit the limitless energy of sunshine to degrade organic compounds is through photocatalytic technology [30–33].

To the best of our knowledge, no activity has been recorded in which the effect of HA on the physical properties and photocatalytic activity of ZnO films was investigated by the degradation of methylene blue dye under UV light. Therefore, in this study, ZnO films with and without HA were prepared by the SILAR method. Structural, morphological, electrical, and photocatalytic properties were investigated using advanced analytical techniques.

## 2. Experimental details

In this experimental process, we produced bare and hyaluronic acid (HA) added nanostructured semiconductor ZnO thin films as a function of the HA concentration in the growth bath by the low-cost and easy SILAR method. 0.1 M concentrations of Zinc (II) acetate dihydrate ($C_4H_{10}O_6Zn$, $\geq$ 99.0 %, Merck) salts were dissolved in 100 mL of deionized water to obtain a $Zn^{+2}$ solution. The pH of the growth bath was adjusted to $\approx$ 12.0 by adding ammonia ($NH_4OH$). This pH value was chosen on the strength of our earlier experience on the influence of pH values on SILAR-fabricated nanostructured metal-oxide samples [34,35]. The temperature of the solution was increased to 85 °C and continued steady at this range during the fabrication process. Next, we immersed the cleaned soda-lime glass substrates in the solution for 20 s, followed by another 20 s in deionized water at 85 °C. These courses were repeated 12 times to obtain thick metal oxide-based ZnO films and powders. Hyaluronic acids are energetically stable, which is partially attributed to the stereochemistry of their component disaccharides. To examine the influence of the hyaluronic acid content on the ZnO films, three series of samples were synthesized. The fabricated ZnO thin films and powders were annealed at 350 K for 1 h in a controlled oxygen environment.

The crystalline structures of the fabricated materials were examined using an X-ray diffractometer (Cu Kα radiation, λ = 1.540056 Å). In order to investigate the surface morphology, a JEM-5610 LV field emission scanning electron microscope (FE-SEM) was used. Brunauer-Emmett-Teller (BET) (Quanta-chrome, US) was used to analyze the surface area of the synthesized samples. Approximately 0.9 g of NPs powder was placed in the tube and allowed to degas at 75 °C for 3 h. The $N_2$ absorption-desorption isotherms of the samples were then measured. The chemical bonding states of the nanostructured ZnO samples were determined by Fourier transform infrared spectrometry (FTIR) at room temperature. Room- temperature photoluminescence (PL) measurements of the samples were performed on an Edinburgh Instruments FS5 model fluorescence spectrofluorometer with an excitation wavelength of 374 nm. The emission spectra were obtained in the wavelength range of 450–600 nm. The electrical performance of the thin film samples was characterized using a computer-controlled Wonatech ZiveSP1 potentiostat in the dark at 27 °C. In order to determine the comprehensive electrical resistivity of the grown samples, the transfer length method (TLM) was applied. Data management for the SMU and all calculations were conducted using VEE Pro-based SeCLaS software [36,37].

The photocatalytic efficiency of the bare ZnO-NPs and the HA (3.0 % and 5.0 % HA: ZnO-NPs) added ZnO-NPs was determined by degradation of the MB solution under UV light irradiation following the procedure. Briefly, 10 ppm solutions of MB were prepared in distilled water, and the pH of these solutions was carefully adjusted with NaOH. 20 mg of each bare ZnO-NPs, 3.0 % HA:ZnO-NPs, and 5.0 % HA:ZnO-NPs was added separately to each 30 mL aliquot of dyes and stirred for 20 min in the dark to maintain adsorption-desorption equilibrium. After that, each mixture was exposed to UV light every 10 min' exposure, and 3 mL of the solution was collected after that and centrifuged to remove the catalysts (3000 rpm, 4 min). Absorbance values were recorded at 665 nm for MB using a UV–vis spectrophotometer (Shimadzu UV-1201), and UV-light (3 W, 395–400 nm) was applied as the UV source (Fig. 1). After 60 min of UV light exposure, the color of the dye solutions significantly decreased.

The absorbance data were used to determine the degradation percent (D%) of MB using the following equation [33,38,39]:

$$D\% = (A_0 - A_t)/A_0 x100 \quad (1)$$

where $A_0$ and $A_t$ represent the initial and after t minutes of reaction/irradiation values of mixture, respectively. Based on Beer-Lambert's law, these values are proportional to $C_0$ and $C_t$, where $C_0$ and $C_t$ are the dye concentration before irradiation and the final concentration of dye after each regular interval. The photo-degradation reaction rate (k) of the MB contaminant was estimated according to the Langmuir-Hinshelwood (first-order kinetic) model [33,38,40]

$$\ln(A_t/A_0) = \ln(C_t/C_0) = -kt \quad (2)$$

The photo degradation rate constant (k, $min^{-1}$) was estimated from the slope of the linear fit of the plot of ln ($C_0/C_t$) vs. t as a result of the obtained data.

## 3. Results and discussion

The surface morphologies of ZnO thin films with and without HA were investigated by FE-SEM analysis, as shown in Fig. 2(a–c). The rod-like structure of ZnO in the absence of HA is shown in Fig. 2(a). In the presence of 3.0 % or 5.0 % HA in the reaction solution, the surface structures of the ZnO thin films become cauliflower- and honeycomb-like structures, respectively (Fig. 2(b,c)). It can be seen in Fig. 2(c) that the FE-SEM images of HA-mediated ZnO films generally show a highly porous structure as the percentage of HA increases. HA

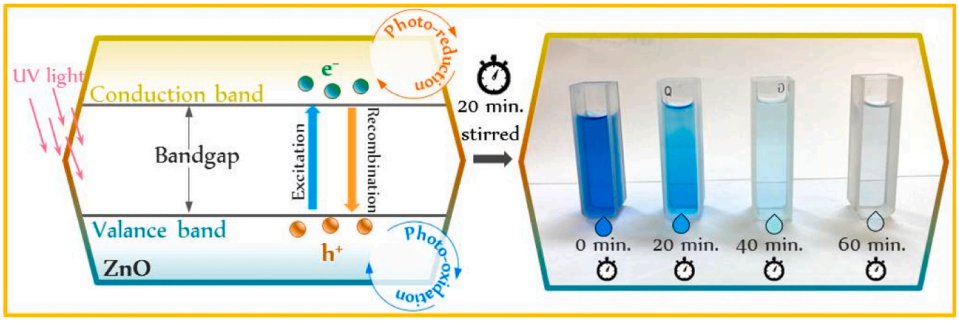


**Fig. 1.** Schematic of the photocatalytic degradation procedure (photo taken from MB + 3.0 % HA:ZnO NPs and the sample was stirred for 20 min in the dark to maintain the adsorption-desorption balance before exposure to UV light).

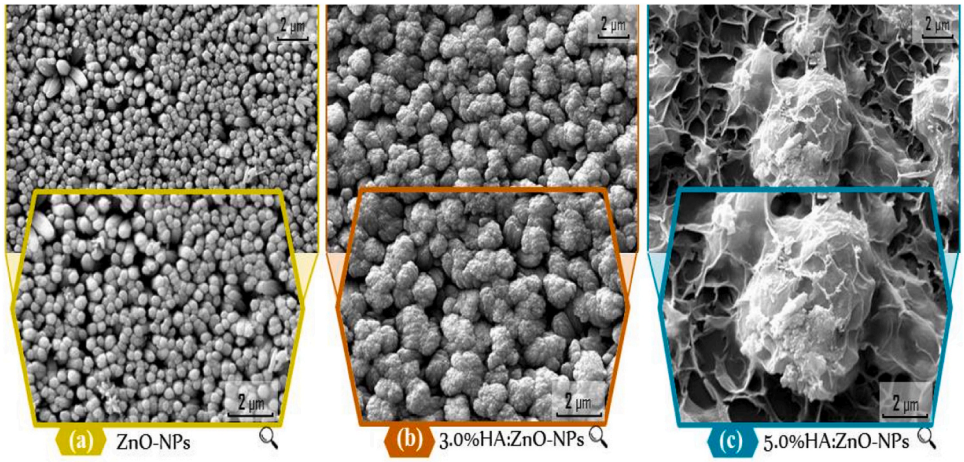


**Fig. 2.** Surface morphologies of fabricated ZnO thin films with and without HA. The rod-like structure of ZnO in the absence of HA is shown in Fig. 2(a). In the presence of 3.0 % or 5.0 % HA in the reaction solution, the surface structures of the ZnO thin films become cauliflower- and honeycomb-like structures, respectively (Fig. 2(b,c)).

significantly affected the surface morphology of the ZnO films with which it interacted, resulting in a structure with increased porosity. This morphological change may be due to properties such as HA's ability to form hydrogels and retain water. In other words, HA's capacity to create hydrogels results in a highly hydrated and porous surface morphology [41–44]. Due to its structure, which is a polysaccharide made up of repeating disaccharide units of glucuronic acid and N-acetylglucosamine, HA can have different surface morphologies based on its molecular weight and concentration [42,45–48].

EDS is a powerful analytical technique that can be used to analyze

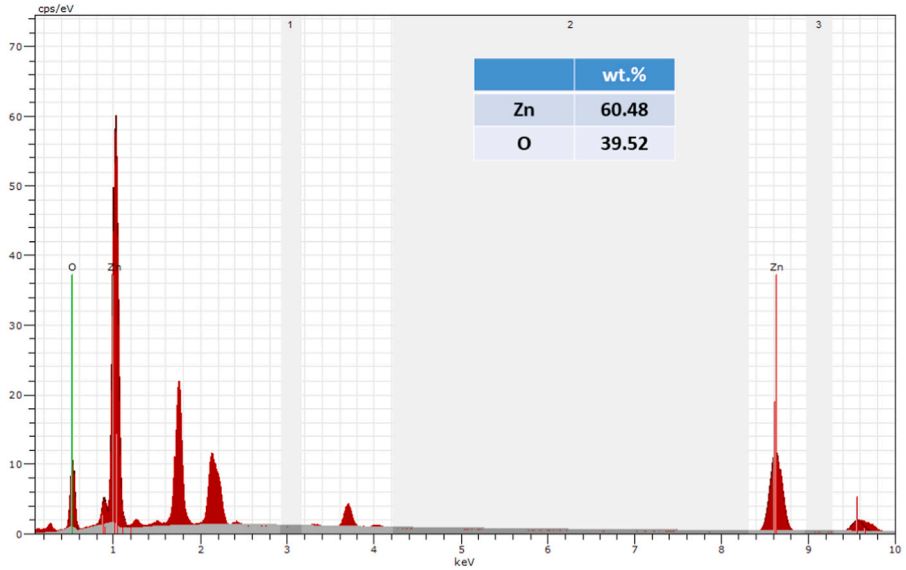


**Fig. 3.** EDS spectrum of nanostructured ZnO film.

the elemental composition of thin films. The EDS method was used to analyze the chemical composition of the ZnO NPs. The EDS spectrum of the bare sample is shown in Fig. 3. The presence of Zn and O peaks in the ZnO film is confirmed by the EDS spectrum shown in Fig. 3. The weight percentages of the ZnO films are shown in Fig. 3.

AFM is a common technique that can generate a topographic image of a film surface by providing information about the surface properties of ZnO NPs as a function of HA. The surface roughness (Sa) and root mean square (Sq) values of the ZnO film surfaces are listed in Table 1.

The ZnO nanoparticles containing HA exhibited a rougher structure than the pure sample, as shown in the AFM images (Fig. 4). The increase in surface roughness in the interaction between HA and ZnO may result from the chemical interaction between the functional groups of HA (such as hydroxyl, carboxyl, and amine groups) and the ZnO surface, as well as phase separation between HA and ZnO due to their different chemical and physical properties during the reaction. In addition, this change may be caused by mechanical stress and thermal processes such as annealing, which may occur between the addition of HA to the reaction bath and ZnO [25,49–51]. As a result, both FE-SEM and AFM images revealed morphological changes with increasing HA content in the growth solution.

The crystalline structures of the fabricated ZnO-NPs were examined by X-ray diffraction (XRD). Fig. 5 shows the XRD spectra of the ZnO NPs treated with HA. The obtained XRD patterns can be indexed as highly crystalline hexagonal wurtzite nanostructured ZnO form (Joint Committee on Powder Diffraction Standards (JCPDS) card, no 36-1451).

No diffraction peaks belonging to other impurities were observed in the XRD patterns; thus, it can be assumed that bare hexagonal-phase nanostructured ZnO structures were fabricated using this low-cost and simple solution-based technique. The diffraction peak intensities decreased with increasing HA content in the growth solution for all the orientations. This can be elucidated by the change in crystallization induced by the alteration in nucleation speed and centers from homogenous to heterogeneous solution components [52–54].

The XRD spectra of the manufactured ZnO-NPs exhibit dominant, sharp, and intense diffraction bands, implying good crystallinity of ZnO-NPs structures. The average crystallite sizes of the samples were estimated from Scherrer's formula (given by Eq. (3)) using the half-wide full maximum (HWFM) intensity of the (100), (002), and (101) peaks. The Debye-Scherrer's equation is given by [55,56]:

$$D = \frac{K\lambda}{\beta\cos\theta} \tag{3}$$

where D is the estimated crystallite size at the nanometer scale, $K$ is a numerical factor, $\lambda$ wavelength of Cu-Kα radiation, $\beta$ full width half maxima in radian, and $\theta$ Bragg's angle for the X-ray. The estimated average crystallite sizes were in the range of 25.20 nm (for bare ZnO-NPs) to 20.20 nm (for 5.0 % HA:ZnO-NPs). The estimated sizes of the grown samples are tabulated in Table 2.

These crystalline changes also showed good agreement with the FE-SEM observations. The surface morphologies of the prepared thin-film materials were compact, as evidenced by the FE-SEM images (see Fig. 2). The XRD diffraction and FE-SEM results clearly demonstrate effective evolution of the crystalline structure and morphology of the samples. Additionally, the obtained film thickness results show that the thickness increased approximately threefold with 3.0 % HA added and approximately fourfold with 5.0 % HA.

Fig. 6 shows the $N_2$ adsorption–desorption isotherms for bare ZnO, 3.0 % HA: ZnO, and 5.0 % HA:ZnO. According to the IUPAC classification, the nitrogen adsorption isotherms in ZnO are classified as type IV, and the adsorbed and desorption are classified as type H3 for all samples. The forms of the steepness and isotherms were not affected by the HA content. The type IV isotherm is generally associated with capillary condensation in its mesopore. The H3-type hysteresis loop is characterized by a steep adsorption branch and a more gradual desorption branch, and it does not exhibit any limiting adsorption behavior at high $P/P_0$ values. This asymptotic increase in relative pressure is usually associated with aggregated particles, as seen in the FE-SEM images (Fig. 2.). The average pore sizes and volumes estimated by applying the Brunauer-Emmett-Teller (BET) method to the isotherms of the samples are presented in Table 3.

**Table 1**
Surface roughness (Sa) and root mean square (Sq) values of ZnO film surfaces.

| Sample name | Sa (nm) | Sq (nm) |
|---|---|---|
| **Bare ZnO-NPs** | 70.05 | 91.61 |
| **3.0 % HA: ZnO-NPs** | 305.99 | 380.64 |
| **5.0 % HA: ZnO-NPs** | 360.69 | 446.37 |

The table shows that the surface area (BET) of bare and HA-added ZnO NPs decreases with increasing HA content to a certain degree, while the pore volume decreases appreciably. However, when the HA content increased, the pore volume and surface area increased, and the values were close to those reported in the literature [57,58].

The diameters of bare and HA-added ZnO NPs can be calculated using the following equation:

$$d_{BET} = 6000/\rho S \tag{4}$$

where $d_{BET}$ is the mean crystalline size (in nm), ρ is the estimated density of ZnO (5.60 g/cm$^3$), and S is the specific surface area determined from the isotherm (see Table 3) [59–61]. The agglomerations in the ZnO nanoparticles were indicated by the inconsistency in the crystalline size as determined by the BET method and by the XRD Scherrer formula. The agglomeration coefficient is the ratio of the sizes of the crystallites, and higher values suggest that agglomeration occurs more readily [58–60].

Agglomeration is a confining factor on the surface area, and a higher surface area material is beneficial for superior photocatalytic activity. This may explain the decrease in photocatalytic efficiency with HA doping, but no correlation was observed with the parameters related to photocatalytic degradation (such as TON, TOF, %D, and k values), and the sample with the largest surface area has not the highest catalytic degradation performance. Thus, we conclude that the specific surface area is not the only factor influencing the photocatalytic degradation performance of metal oxide catalysts [62,63].

The Pore-Size Distributions (PSD) of the samples (Fig. 7), obtained from $N_2$ desorption isotherms using the NLDFT approach exhibit more strict differences in the porosity of the fabricated materials [64,65]. These distribution functions are very similar to each other. All samples exhibited the presence of mesopore with a characteristically prominent peak between 20 and 25 nm. In addition, characteristic cavities with pore sizes between 13 and 40 nm is clearly observed. In addition, very weak volume pore size values demonstrate remarkable microporosity (below 10 nm) and are difficult to characterize properly by low-temperature nitrogen adsorption [64].

The different vibration modes of the HA:ZnO-NPs were studied by Fourier transform infrared spectroscopy (FT-IR). The size, shape, and clustering of the nanoparticles influence the behavior of FT-IR [66]. The FT-IR spectra of the samples composed of bare ZnO NPs and-NPs, samples containing 3.0 % and 5.0 % HA were displayed in Fig. 8. These materials were tested to verify their structural characteristics. The FTIR spectra of the produced samples, measured in the wavenumber range of 500–4000 cm$^{-1}$, indicated the presence of several vibrational modes.

Typically, metal oxide nanoparticles have distinct absorption peaks in the fingerprint area (below 1000 cm$^{-1}$) as a result of stretching vibrations. The vibrations are result of the interatomic vibration modes of metal oxides [67,68]. The absorption peak observed at 897 cm$^{-1}$ is attributed to the specific stretching mode of the Zn—O bond. The absorption peaks at 3732 and 3622 cm$^{-1}$ are often ascribed to the stretching modes of O–H in surface adsorbed water molecules or the hydroxyl groups in Zn–OH. The absorption of atmospheric carbon dioxide by metallic cations can account for the prevalence of absorption

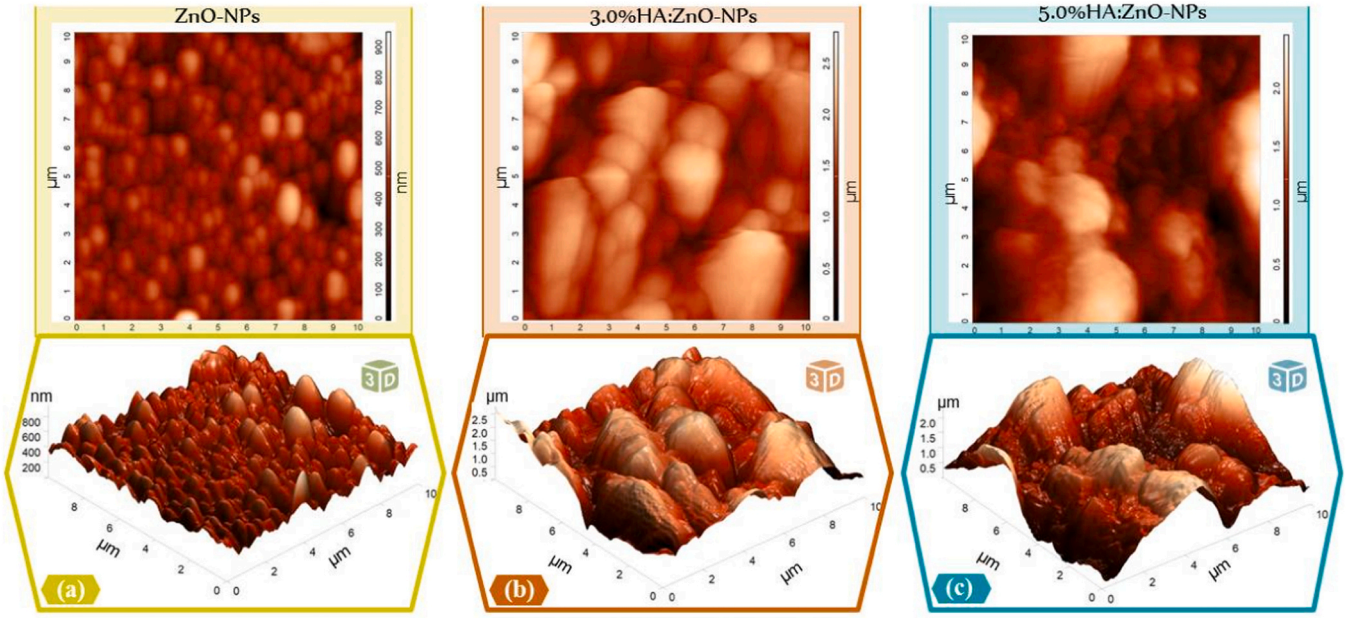


**Fig. 4.** 2D and 3D AFM images of nanostructured ZnO thin films with different HA contents.

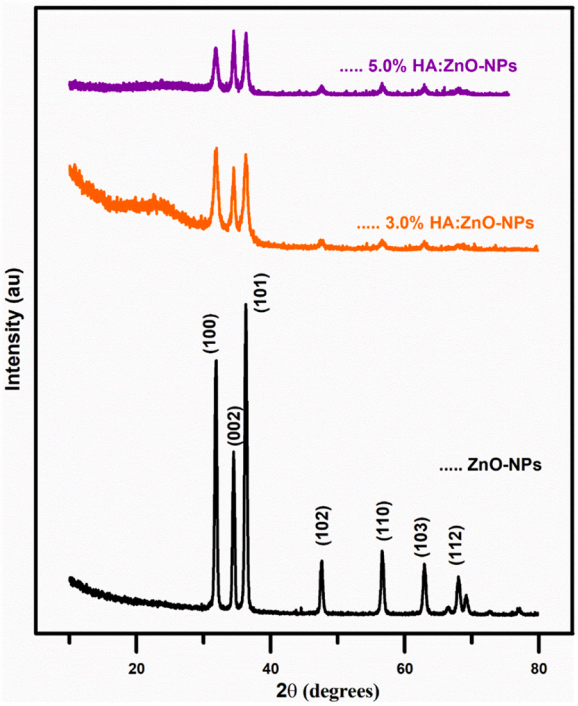


**Fig. 5.** XRD spectra of the bare ZnO-NPs and HA (3.0 % and 5.0 %) mediated ZnO-NPs.

**Table 2**
Crystallite sizes, film thicknesses, and full width at half maximum (β) values of metal-oxide semiconductor ZnO samples.

| Sample name | Crystallite size (nm) | Film thickness (μm) | Full width at half maximum (β) |
|---|---|---|---|
| **Bare ZnO-NPs** | 25.20 | 0.59 | 0.4330 |
| **3.0 % HA: ZnO-NPs** | 27.30 | 1.95 | 0.3542 |
| **5.0 % HA: ZnO-NPs** | 20.20 | 2.11 | 0.5038 |

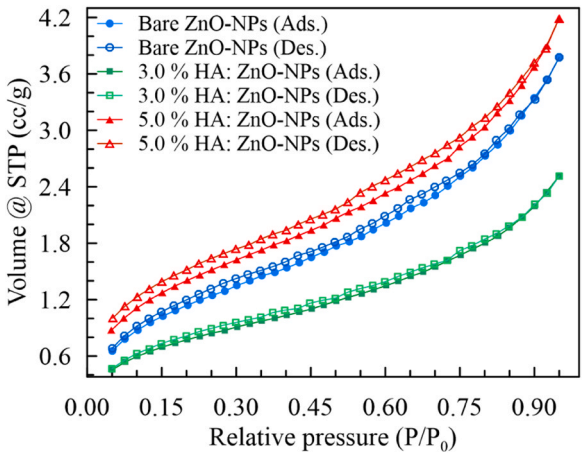


**Fig. 6.** $N_2$ adsorption–desorption isotherms of bare and HA-doped ZnO NPs: Filled symbols represent adsorption; open symbols, desorption.

**Table 3**
BET analysis surface areas and porosities of bare and HA-mediated ZnO NPs.

| Sample name | DFT method | | BET summary |
|---|---|---|---|
| | Pore volume (cc/g) | Surface area ($m^2$/g) | Surface area S ($m^2$/g) |
| **Bare ZnO-NPs** | 0.005 | 2.742 | 4.439 |
| **3.0 % HA: ZnO-NPs** | 0.003 | 1.898 | 2.987 |
| **5.0 % HA: ZnO-NPs** | 0.006 | 3.595 | 5.204 |

peaks at 2356 $cm^{-1}$ [69]. Further bands observed at approximately 3000–2900 and 1600–1000 $cm^{-1}$, which were previously ascribed to chemical bonding, could potentially have arisen due to the deformation and bending vibrations of CO and $CH_2$-$CH_3$ molecules that were chemically or directly absorbed [34,70]. The following vibration modes were identified as a consequence of different structural bonds: 1521 and 1026 $cm^{-1}$ for CO stretching vibrations induced by air and 2951, 2885,

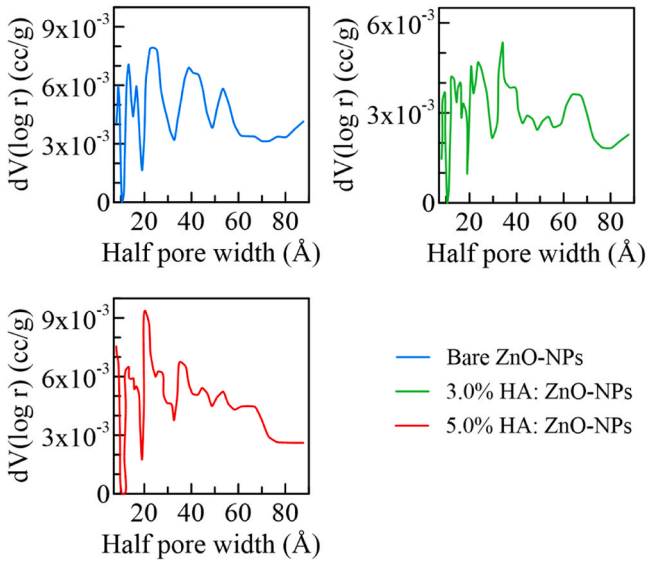


**Fig. 7.** Pore-size distributions of the fabricated samples calculated using the NLDFT approach (equilibrium model).

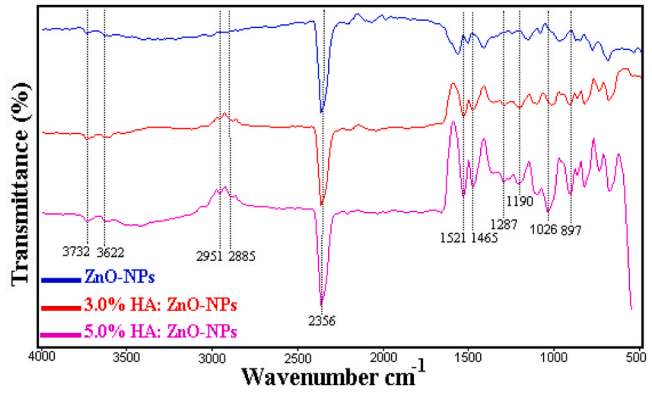


**Fig. 8.** FT-IR spectra of the bare ZnO-NPs and HA (3.0 % and 5.0 %) mediated ZnO-NPs.

1465, and 1287 $cm^{-1}$ for $CH_2$-$CH_3$ vibrations.

By investigating the regions associated with the vibration of ZnO bond in FT-IR spectra, it was possible to ascertain the optical phonon frequency ($\nu_0$). $\nu_0$ represents the frequency of the optical phonon in hertz (Hz), $\nu$ denotes the wave number in reciprocal centimeters ($cm^{-1}$), and λ signifies the wavelength in centimeters (cm). Equations were used to calculate the values of $\nu_0$ and Debye temperature $\theta_D$ based on the observed vibration of ZnO bonds. $c = \lambda\nu_0 = \nu_0/\nu$ and $h\nu_0 = k_B\theta_D$, where $h$ and $k_B$ are the Planck's constant and Boltzmann constant [71].

$$\nu = \frac{1}{2\pi c}\left(\frac{k}{\mu}\right)^{1/2} \quad (5)$$

ZnO's force constant can be determined utilizing Eq. (5). Here, k is the force constant, c is the speed of light ($3.00 \times 10^{10}$ cm/s) and μ is an effective mass of ZnO, given by $\mu = \frac{m_1 \times m_2}{m_1 + m_2}$, where $m_1$ and $m_2$ are the atomic weights of bounded atoms. The calculated vibrational parameters are listed in Table 4.

PL is a preferable method to research the crystalline quality and presence of impurities in catalysts and provides knowledge about the different energy states available between the conduction band (CB) and valence band (VB) responsible for irradiative recombination due to the exciton-exciton collision (near-band-edge emission, NBE) and deep level (DL) emission (caused by intrinsic point defects and surface defects) in ZnO [72–76]. In particular, defining the recombination mechanism and time dependency of it provides an explanation of carrier dynamics, which is directly related to conductivity and photocatalytic activities [76–78]. Usually, the PL spectra of nanostructured ZnO materials are composed of two peaks: one related to NBE emission in the UV range and the other to defect level emission in the visible region. The first strong peak in the UV-emission region (at 380 nm) was attributed to near-band-edge emission through exciton-exciton collision processes. The other peak is in the visible region and presumably comes from electron-hole recombination at a deep level caused by intrinsic point defects and surface defects, oxygen vacancies ($V_O$), zinc interstitials ($Zn_i$), zinc vacancies ($V_{Zn}$), oxygen interstitials ($O_i$), anti-site oxygen ($O_{Zn}$), and the incorporation of hydroxyl groups in the crystal lattice during solution growth [72,74,77,79].

Fig. 9 presents the PL spectra of the fabricated materials measured under room conditions. The visible blue-green emission at 460.7 nm was attributed to the radiative transition of an electron from the shallow donor level of $Zn_i$ to the acceptor level of neutral or singly ionized $V_{Zn}$ defects [74,75,80]. The blue and green emission peaks (between 468.4 nm and 498.7 nm) originated from the electron transition from the shallow donor level of $V_O$ to the valence band (which occurs in three diverse charge states: the singly ionized, the doubly ionized and the neutral) and the electron transition from the shallow donor level of $Zn_i$ to the valence band [77,79,81,82]. It is common to associate the green-yellow emission at 545.3 nm with the defect of $Zn_i$ and anti-site O ($O_{Zn}$) [83]. In addition, the morphology of the nanostructures is associated with sub-bandgap emission in ZnO. A blue-green emission at 460.7 nm and a green emission at approximately 545.3 nm were observed in the literature for honeycomb-like nanoparticles, as indicated by the SEM results [77,80]. Finally, the peak observed in the orange region (~ 582.8 nm) is attributed to the radiative recombination of localized electrons with deeply trapped holes in the $O_i$ located at 2.14 eV below the conduction band, which results in orange luminescence [82,

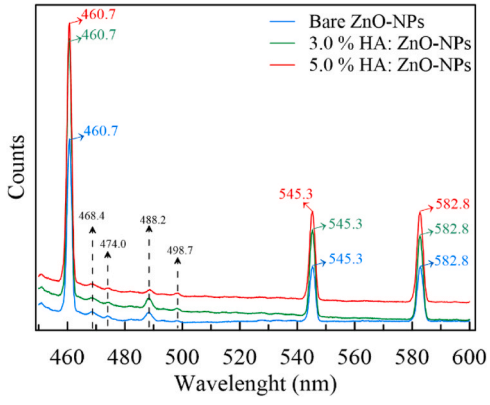


**Fig. 9.** Photoluminescence spectra of bare and HA-mediated ZnO nanoparticles.

**Table 4**
FT-IR bands, wavenumber, effective mass, force constant, optical phonon frequency, and Debye temperature value for nanostructured ZnO.

| Sample | Wavenumber ($cm^{-1}$) | Effective mass ($10^{-26}$ kg) | Force constant k (N/cm) | Optical phonon frequency, $\nu_0$ (Hz) $10^{13}$ | Bending Debye temperature $\theta_D$ (K) |
|---|---|---|---|---|---|
| ZnO | 897 | 2.1343 | 6.1018 | 2.691 | 1291 |

84].

The time-resolved photoluminescence (TRPL) system was used to investigate the excitonic emission and related carrier lifetime (τ) of the bare ZnO NPs and HA doped ZnO NPs. Fig. 10 shows the TRPL decay profiles of the samples at room temperature. All bare and HA-doped ZnO NPs exhibited double-exponential behavior, which strongly implies the existence of two distinct decay and/or capture mechanisms in the emission spectra. Thus, the double-exponential function fits well ($R_{(t)} = B_1 e^{-t/\tau_1} + B_2 e^{-t/\tau_2}$) to explain the emission (Fig. 11). The fast decay component ($\tau_1$) describes the radiative lifetime of the free photo-generated carriers, and the slow decay component ($\tau_2$) is attributed to electron recapturing and nonradiative recombination processes. The fast decay time was nearly constant for bare and 5.0 % HA:ZnO NPs and slightly increased for the 3.0 % HA:ZnO NPs. However, the amplitude ratios (AR = $B_1/B_2$) were 120.15, 108.58, and 90.19 for bare ZnO-NPs, 3.0 % HA:ZnO-NPs, and 5.0 % HA:ZnO-NPs, respectively. This ratio indicates that electron recapturing and nonradiative recombination processes become the dominant mechanisms in the carrier's kinetic behavior, as mentioned in the literature [79]. This phenomenon may also be correlated with the charge-transfer interactions in aqueous solutions of MB and HA.

The electrical properties of bare and HA-added ZnO-NPs thin film samples were examined by the Transfer Length Method (TLM). To perform I-V measurements, Au contact patterns were prepared on thin films by the physical vapor deposition (PVD) method. In each sample, there are four Au contact patterns with different distances between them, represented by numbers 1, 2, 3, and 4. I-V measurements were taken by connecting two contacts from patterns 1–2 (@12link), 2–3 (@23link), and 3–4 (@34link), respectively.

A schematic representation of the experimental system and a photographic image of the Au contact patterns on bare ZnO thin films are shown in Fig. 12. To obtain the electrical parameters using the TLM method, Eqs. (6) and (7) given below were used.

$$R_c = \frac{R_{Sk} L_T}{w} \coth(d/L_T) \tag{6}$$

$$L_T = \sqrt{\frac{\rho_c}{R_{Sk}}} \tag{7}$$

The width of the patterns is represented by $w$ and the length by $d$. $R_{Sk}$ is modified sheet resistance under the contact. From these equations, important electrical parameters of thin film samples, such as effective transfer length ($L_T$), specific contact resistance ($\rho_c$) and total contact resistance ($R_c$) can be obtained. Thus, detailed information can be obtained about the homogeneity, conductivity, and overall performance of thin films [85]. Details of the method can be found in previous studies [34,86].

I-V measurements of the thin film samples were carried out in potentiostatic I-V mode at a 50 mV/S scan rate by connecting two

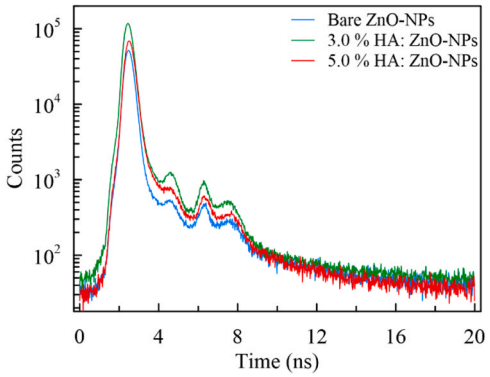


**Fig. 10.** Time-resolved PL spectra of bare and HA-mediated ZnO nanoparticles.

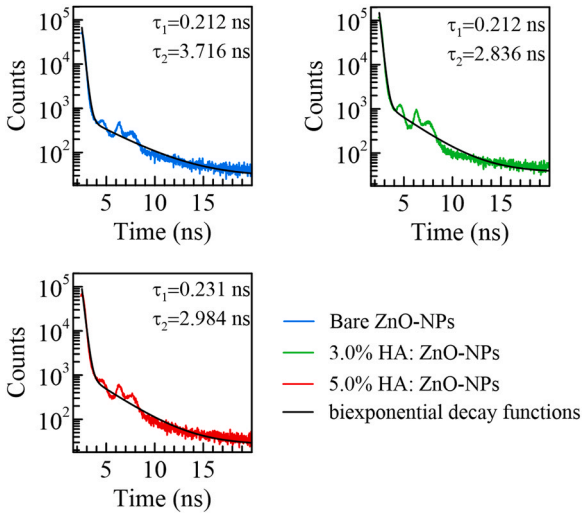


**Fig. 11.** Fitted time-resolved PL spectra of the fabricated samples. The TRPL analysis data were fitted according to the differential rate (biexponential decay function) law.

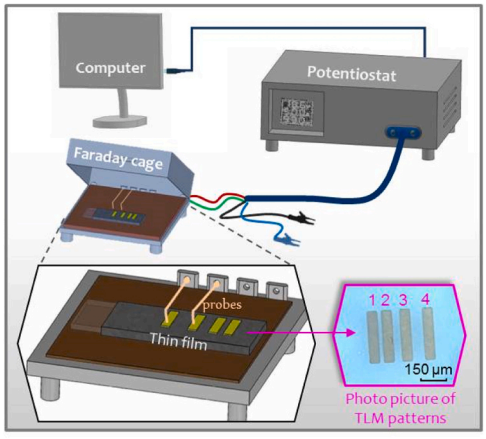


**Fig. 12.** Experimental setup of the I-V measurement system and an example photographic image of contact patterns from bare ZnO for the TLM method.

electrodes and using a potentiostat. The current ranges were set to 1 μA for bare ZnO and 10 nA for 3.0 %HA:ZnO-NPs and 5.0 % HA:ZnO-NPs to obtain more sensitive measurements. Because the current values of the HA-added samples were lower at the same potential difference compared to bare ZnO. Fig. 13-a–c show the I-V characteristics of the bare ZnO, 3.0 % HA: ZnO, NPs and 5.0 % HA: ZnO NPs samples, respectively. From these I-V measurement results, series resistance values were calculated for the @12, @23, and @34 links. Fig. 14 a–c show the series resistance values of bare ZnO-NPs, 3.0 %HA:ZnO-NPs and 5.0 %HA:ZnO-NPs samples, respectively. Resistance values increase in all samples as the distance between contacts increases. This may provide positive information about film homogeneity. It can be concluded that the film thickness does not significantly change in the region of the TLM patterns or spreads homogeneously. Because the film thickness and the change in distance may have different effects on the change in series resistance. The effects of film thickness on resistance were mentioned in the previous study [87].

It has been reported that impurities such as organic compounds that affect the crystallinity quality of ZnO-NPs can alter their photocatalytic performance by changing the absorption of light and transport efficiency of photogenerated charge carriers [88]. On the other hand, it has also been reported that phosphonic acid-modified ZnO films have low

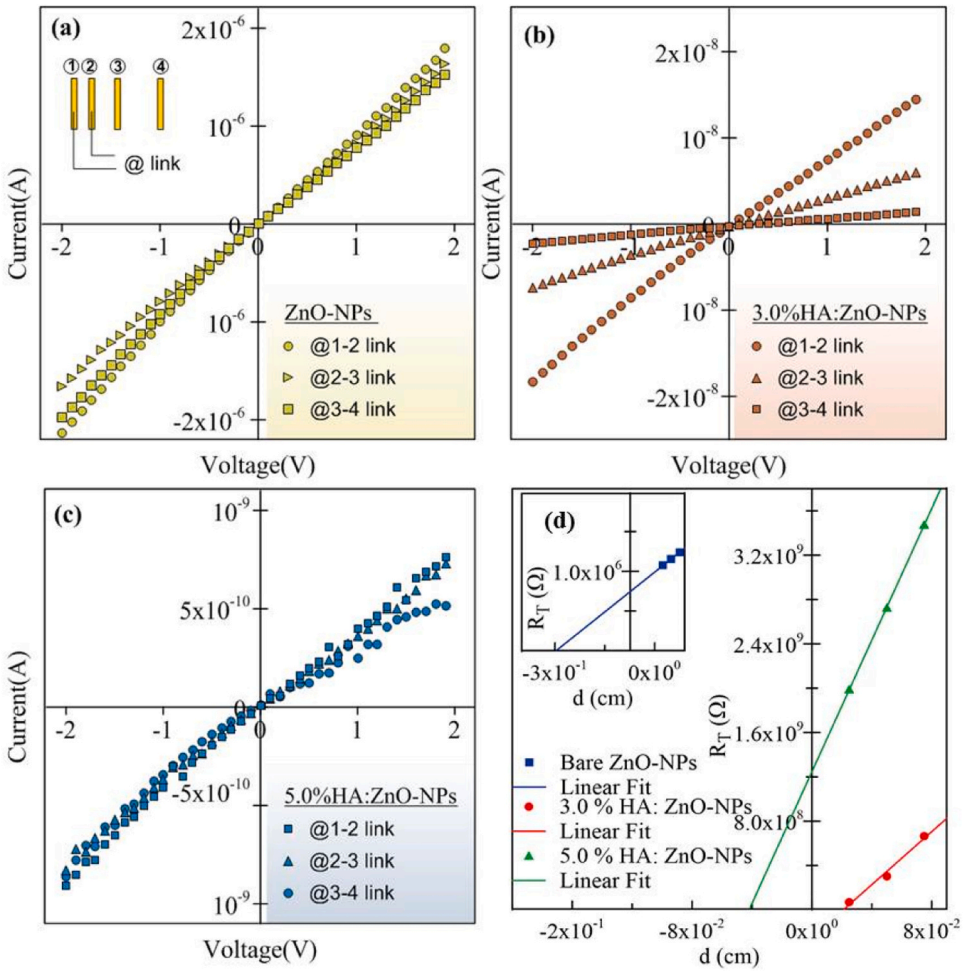


**Fig. 13.** I–V characteristics of the bare ZnO-NPs and HA (3.0 % and 5.0 %) mediated ZnO-NPs.

conductivity in electron transport/hole blocking layer [89]. The change in specific contact resistance upon doping is shown in Fig. 14-d. The value, which was 1.13 × $10^4$ Ω $cm^2$ for bare ZnO, increased to 4.56 × $10^6$ Ω $cm^2$ with 5.0 % HA. The values of the electrical parameters obtained for the fabricated ZnO thin films are given in Table 5.

$L_T$ values decrease as the HA content increased. While it is 14.81 μm for Bare ZnO-NPs decreased to 2.10 μm for 5.0 % HA: ZnO-NPs. $R_c$ values increase as the HA content in ZnO increased. The highest Rc value was 0.623 × $10^9$ Ω for 5.0 % HA: ZnO-NPs. It seems that HA doping of ZnO has a significant effect on the electrical parameters of the material. The increased electrical resistance with the addition of HA to ZnO may be due to the increase in the organic compound density in the film (which can also be observed in the morphological structure), and this increase may also have changed the photocatalytic effect by regulating the formation of electron-hole pairs in the photons absorbed by ZnO.

Alterations in the structure and size of particles in metal-oxide thin film materials have great importance for assaying their conductivity performance. The FE-SEM images of bare ZnO and HA are shown in Fig. 2. This confirms that the addition of HA is the principal reason for the transformation from rod-like to cauliflower-like growth. It has been reported that the electrical conductivity of nanostructured oxide materials is dictated by carrier mobility and principally affected by electron scattering at the surface of nanostructures or grain boundaries. To interpret the catalytic performance of ZnO, its stability and charge carrier dynamics must be considered in common photocatalytic implementations. From this viewpoint, the conductivity of ZnO-NPs is strongly affected by the addition of HA. Similar outcomes to the conductivity results, related to particle size and morphology, have been reported in previous studies on nanostructured metal oxide materials [90–92].

The electrical performances of the samples influenced the desired photocatalytic reactions. Hence, optimizing both the electrical conductance and photocatalytic efficiency of the synthesized materials can be employed to achieve the desired properties. If materials have low resistivity, they can induce the mobility of these charge carriers, which leads to their participation more effectively in photocatalytic abilities. Hence, both the crystalline and electronic structures of metal oxides play an important role in the degradation of pollutants [11,93].

In a similar manner, the relationship between particle size and the catalytic efficiency of the fabricated materials has been described in the literature. Adjustments to the particle size and distribution of semiconductor-based nanoscale photocatalysts are crucial for optimizing their catalytic efficacy [94]. At the nanoscale, as the particle size changes, the surface-area-to-volume ratio of the materials changes. If particles are nano-sized, they have more active sites available per unit mass for catalysis, thereby boosting the catalytic activity. Nanostructured semiconductors commonly have a larger optical bandgap energy, allowing them to absorb higher-energy photons in the visible region, which is more effective for initiating photocatalytic reactions. Meantime, nano-scale particles can absorb more visible light owing to their extensive surface area, which promotes photon absorption and boosts electron excitation, which is an important factor in the photocatalytic process [95,96].

The photocatalytic decolorization of MB with manufactured bare ZnO and HA (3.0 % and 5.0 %) mediated ZnO-NPs was measured by UV–vis spectra, and the results are presented in Fig. 15. The initial

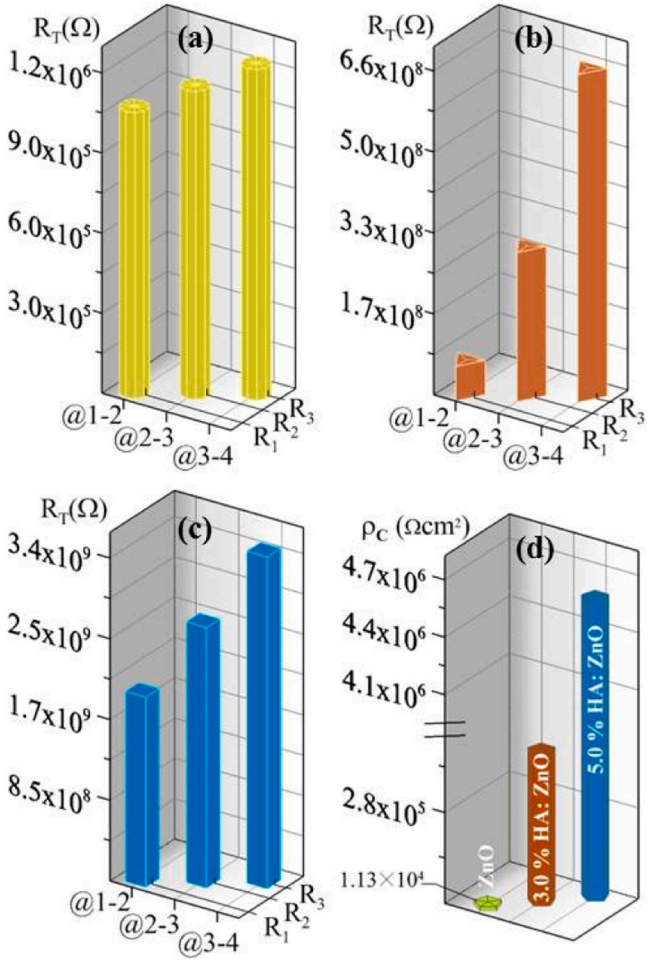


**Fig. 14.** Series resistance values of (a)bare ZnO-NPs, (b) 3.0 % HA, (c) 5.0 % HA-mediated ZnO-NPs and (d) specific contact resistance of the samples.

**Table 5**
Electrical parameters of the ZnO thin films obtained by the TLM method.

| Sample | $R_1$ ($\Omega$) | $R_2$ ($\Omega$) | $R_3$ ($\Omega$) | $L_T$ ($\mu$m) | $\rho_c$ ($\times 10^5$ $\Omega$ cm$^2$) | $R_c$ ($\Omega$) |
|---|---|---|---|---|---|---|
| **Bare ZnO-NPs** | 1.073 × $10^6$ | 1.155 × $10^6$ | 1.240 × $10^6$ | 14.805 | 0.113 | 0.495 × $10^6$ |
| **3.0 % HA: ZnO-NPs** | 6.993 × $10^7$ | 3.034 × $10^8$ | 6.674 × $10^8$ | 1.048 | 4.597 | 0.125 × $10^9$ |
| **5.0 % HA: ZnO-NPs** | 1.990 × $10^9$ | 2.728 × $10^9$ | 3.475 × $10^9$ | 2.098 | 45.624 | 0.623 × $10^9$ |

absorption peak at 665 nm systematically declined and became almost transparent after 60 min under UV light irradiation.

The fabricated ZnO-NPs exhibit better photocatalytic activity than HA-incorporated ZnO-NPs under UV light. No synergistic effect of HA on the photocatalytic degradation was observed. However, a reducing effect of HA on the degradation percentage was clearly observed. This is due to its reducing effect on OH ions, which are part of the nature of photocatalytic degradation and form a basic environment, and they could interfere with the photocatalytic activity [33,97–101]. This phenomenon is consistent with the increase in the degradation percentage due to the increase in the HA ratios (Fig. 16).

It is also known that a complex can form between aqueous solutions of MB and HA through charge-transfer interactions, leading to the degradation of MB through photoinduced electron transfer [97]. This

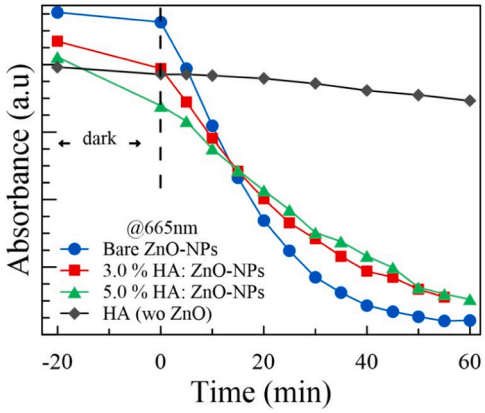


**Fig. 15.** Changes in absorbance values of MB solutions with UV light exposure time: bare HA (◆), bare ZnO-NPs (●), 3.0 % HA: ZnO-NPs (■), and 5.0 % HA: ZnO-NPs (▲).

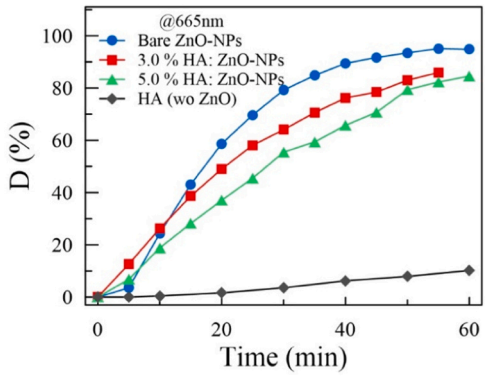


**Fig. 16.** Changes in degradation percent of MB solutions with UV-light exposure time: pure HA (◆), bare ZnO-NPs (●), 3.0 % HA: ZnO-NPs (■), and 5.0 % HA: ZnO-NPs (▲).

charge transfer process is known to enhance photocatalytic degradation via interfacial charge transfer of ZnO doped with highly conductive dopants, such as reduced graphene oxide (rGO) [102]. However, HA is an organic compound and does not contribute to conduction.

The degradation rate constant (k) obtained from linear fits to first-order kinetic plots (Fig. 17.). The degradation rate of pure hyaluronic acid was ~ $1.86 \times 10^{-3}$ min$^{-1}$, which is lower than that of pure ZnO (~ $5.76 \times 10^{-2}$ min$^{-1}$). However, the rate constant values of (3 % and 5 %) HA-doped NPs were between these two values and decreased exponentially with increasing HA concentration (Fig. 18).

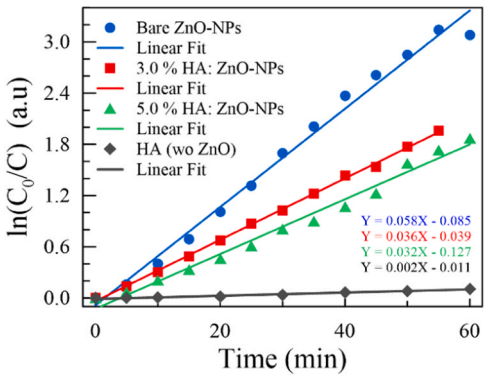


**Fig. 17.** First-order kinetic plots of pure HA (◆), bare ZnO-NPs (●), 3.0 % HA: ZnO-NPs (■), and 5.0 % HA: ZnO-NPs (▲).

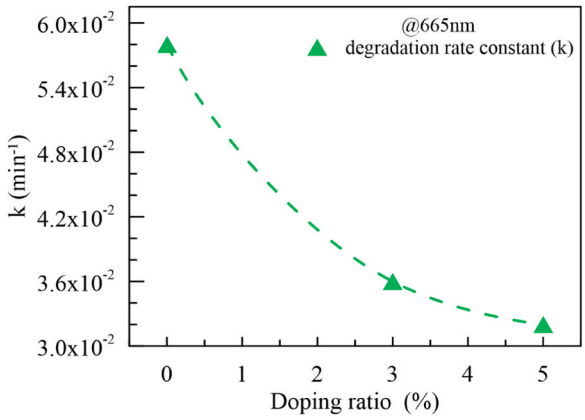


**Fig. 18.** Rate constants of bare ZnO-NPs, 3.0 % HA: ZnO-NPs, and 5.0 % HA: ZnO-NPs.

This indicates that the incorporation of ZnO-NPs with HA has largely influenced the rate constant. In addition, the activity comparison of bare ZnO and HA-implanted ZnO-NPs in terms of the rate constant k was not based on the same surface area of the active photocatalyst but on their total mass.

The photocatalytic degradation of organic dyes, such as MB by metal oxides under light irradiation usually occurs via two main mechanisms [103]. The first mechanism is based on the excitation of metal oxides to create electron ($e^-$) / hole ($h^+$) pairs and subsequent chemical reactions with the surrounding media. The other mechanism is based on the excitation of electrons in the dye molecule, which then becomes an electron acceptor, i.e., a cationic dye radical. Thus, self-degradation or degradation by the reactive oxidation species occurs. The photocatalytic degradation of MB in this work can be represented by the following Eqs. (8)–(10) [104].

$$ZnO + h\vartheta \rightarrow ZnO^* \tag{8}$$

$$ZnO^* + H_2O \rightarrow ZnO^* + H^+ + OH^- \tag{9}$$

$$OH^- + MB \rightarrow intermediate \rightarrow CO_2 + H_2O + mineral\ salts \tag{10}$$

In aqueous HA solutions, a proton detached from the carboxyl group leaves behind a hyalunarate anionic compound. Thus, the presence of additional protons to the protons generated in step (9) leads to the protonation of OH ions in step (10) without interacting with MB, leading to a weakening/decreasing of the degradation process. This process is part of natural, native chemical properties (e.g. neutralizing free radicals) [105].

The term "active site" in heterogeneous catalysis refers to the specific locations on the catalyst surface where the adsorption of reactants occurs and where catalytic reactions are facilitated. Active sites are the specific spots on a catalyst that facilitate the adsorption of reactant molecules and the subsequent catalytic reaction. The presence and characteristics determine the catalyst's efficiency and selectivity. Here, the turnover number (TON) defines a quantitative measure of a catalyst's effectiveness and is simply defined as dividing the total number of product molecules by the total number of active sites (or catalyst molecules) available in the reaction system;[106–108]

$$\mathrm{TON} = \frac{(\%\mathrm{D})(\text{Number of molecules of substrate})}{\text{Number of molecules of catalyst}} \tag{11}$$

This is a key metric in photocatalytic degradation and measures the effectiveness of a catalyst in facilitating a reaction, especially in heterogeneous reactions. In our experiment, 20 mg ZnO ($m_a$ = 81.379 g/mol) contained 16.068 mg Zn as an active site, which corresponded to 24.576 mmol ($m_a$ = 65.36 g/mol). Similarly, a 30 mL, 10 ppm MB solution contains 9.379 × $10^{-7}$ moles as catalyst number. The active sites of the doping molecules were also calculated, taking into account the doping level. We assume that four biding sites (three $OH^-$ and one $–CH_3$ groups) of HA act as acceptors, whereas the remaining molecule was a donor [109,110]. Percentage conversion (D%) or degradation efficiency of MB actually means the extent of the degradation of a substrate molecule, which can be calculated using Eq. (11).

Another useful term is defined as turnover frequency (TOF), which equals the number of reaction cycles taking place in a given time period. This parameter has a time-inverse unit, and it was given by the following equation [107];

$$\mathrm{TOF} = \frac{\mathrm{TON}}{\mathrm{time}} \tag{12}$$

This method provides a more dynamic measure of a catalyst's performance compared to the TON, which is a static count of reactions per active site. The calculated parameters are listed in Table 6. As can be seen, the TON and TOF parameters decrease with increasing doping concentration, which indicates that ZnO NPs are less effective catalysts for HA doping.

## 4. Conclusions

In conclusion, bare and HA-mediated ZnO-NPs were effectively manufactured and characterized using different well-known instrumental techniques. The present study focuses on the investigation of the relationship between the electrical activity and photocatalytic degradation of MB in the presence of ultraviolet light. Both the crystalline and electronic structures of metal oxides play important roles in pollutant degradation. The average crystallite sizes were in the range of 25.20 nm (for bare ZnO-NPs) to 20.20 nm (for 5.0 % HA:ZnO-NPs). The change in the specific contact resistance, which was 1.13 × $10^4$ Ω $cm^2$ for bare ZnO, increased to 4.56 × $10^6$ Ω $cm^2$ with 5.0 % HA in the growth bath. The photocatalytic efficiency of ZnO catalysts is not solely influenced by the specific surface area; agglomeration was observed in the calculated crystalline morphologies. The emissions in the visible region, including blue-green, green, and orange, are likely a result of the recombination of electrons and holes at a deep level emission within the band gap. Furthermore, the amplitude ratio and double-exponential function well fit the decay curves, suggesting that the carrier kinetic behavior is dominated by electron recapturing and nonradiative recombination processes. The degradation results showed that both bare and HA-mediated ZnO nanoparticles were considerably active photocatalysts in the degradation of MB. We hope that these results will provide insight into the design of ecologically safe, nontoxic, and stable nanoscale metal oxide structures emulsified using natural materials in the future.

**Table 6**
Parameters calculated for the photocatalytic degradation process.

| Sample | Active site subs. (× $10^{-4}$ mol) | Active site dopant (× $10^{-6}$ mol) | Total active site (× $10^{-4}$ mol) | (%D) | TON | TOF (× $10^{-3}$ $min^{-1}$) |
|---|---|---|---|---|---|---|
| **Bare ZnO-NPs** | 2.457 | 0 | 2.457 | 95.410 | 0.364 | 6.071 |
| **3.0 % HA: ZnO-NPs** | 2.383 | 1.582 | 2.399 | 88.079 | 0.344 | 5.740 |
| **5.0 % HA: ZnO-NPs** | 2.334 | 2.636 | 2.360 | 84.519 | 0.336 | 5.598 |

* The number of molecules of MB is 9.379 × $10^{-7}$ mol and the time was 60 min.

## CRediT authorship contribution statement

**abdullah akkaya:** Writing – review & editing, Writing – original draft, Software, Formal analysis, Data curation, Conceptualization. **Ebru Karakaş Sarıkaya:** Writing – original draft, Formal analysis, Data curation. **Osman Kahveci:** Writing – original draft, Formal analysis, Data curation. **Raşit Aydın:** Writing – original draft, Formal analysis, Data curation. **Bünyamin Şahin:** Writing – review & editing, Writing – original draft, Supervision, Investigation, Formal analysis, Data curation. **Enise Ayyıldız:** Writing – original draft, Supervision.

## Declaration of Competing Interest

The authors declare that they have no known competing financial interests or personal relationships that could have appeared to influence the work reported in this paper.

## Data availability

Data will be made available on request.

## References


[1] W.K. Kadhim, M.A. Habeeb, Fabrication and tuning the morphological, structural and dielectric characteristics of PVA-PEG-$SiO_2$-$Co_2O_3$ nanocomposite films for nanoelectronics and energy storage devices, Silicon (2024) 1–11.

[2] M.U. Khan, C.M. Furqan, J. Kim, S.A. Khan, Q.M. Saqib, M.Y. Chougale, R. A. Shaukat, M.H. Kang, N.P. Kobayashi, J. Bae, H.-S. Kwok, Asymmetric GaN/ZnO engineered resistive memory device for electronic synapses, ACS Appl. Electron. Mater. 4 (2022) 297–307.

[3] R. Aydın, A. Akkaya, O. Kahveci, B. Şahin, Nanostructured CuO thin-film-based conductometric sensors for real-time tracking of sweat loss, ACS Omega 8 (2023) 20009–20019.

[4] M.M. Alam, A.M. Asiri, M.T. Uddin, M.M. Rahman, M.A. Islam, An alternative electrochemical approach for toluene detection with ZnO/MgO/$Cr_2O_3$ nanofibers on a glassy carbon electrode for environmental monitoring, Rsc Adv. 10 (2020) 44641–44653.

[5] M. Aazza, H. Ahlafi, Investigation of m-NP and p-NP adsorption from single and binary aqueous solutions onto $Al_2O_3$ and HDTMA+/$Al_2O_3$ composite using first derivative UV/Visible spectrophotometry, J. Mol. Liq. 398 (2024) 124220.

[6] J. Ahmed, M. Ubiadullah, M.A.M. Khan, N. Alhokbany, S.M. Alshehri, Significant recycled efficiency of multifunctional nickel molybdenum oxide nanorods in photo-catalysis, electrochemical glucose sensing and asymmetric supercapacitors, Mater. Charact. 171 (2021) 110741.

[7] Z. Golshani, F. Arjmand, S. Maghsoudi, S.M.A. Hosseini, $Fe_2O_3$–NiO doped carbon counter electrode for high-performance and long-term stable photovoltaic perovskite solar cells, J. Mater. Res. Technol. 23 (2023) 2612–2625.

[8] R. Hamed, R.Z. Obeid, R. Abu-Huwaij, Plant mediated-green synthesis of zinc oxide nanoparticles: an insight into biomedical applications, Nanotechnol. Rev. 12 (2023).

[9] A.H. Jaafar, C. Lowe, A. Gee, N.T. Kemp, Optoelectronic switching memory based on ZnO nanoparticle/polymer nanocomposites, ACS Appl. Polym. Mater. 5 (2023) 2367–2373.

[10] R. Ahmad, A. Sohail, M. Yousuf, A. Majeed, A. Mir, M. Aalim, M.A. Shah, P–N heterojunction NiO/ZnO nanowire based electrode for asymmetric supercapacitor applications, Nanotechnology 35 (2024) 065401.

[11] G. Ahmed, W.S. Mohamed, M.F. Hasaneen, H.M. Ali, E.M.M. Ibrahim, Optical, structural, electrical and photocatalytic properties of aluminum doped zinc oxide nanostructures, Opt. Mater. 140 (2023) 113880.

[12] T.M. Rashid, U.M. Nayef, M.S. Jabir, Synthesis of Au/ZnO nanocomposite and Au: ZnO core:shell via laser ablation for of photo-catalytic applications, Mater. Technol. 37 (2022) 2457–2464.

[13] A.M. Mohammad, S.K. Fatah, M.H. Majeed, S.M. Mohammed, S.M. Mohammed, Enhanced antibacterial activity and structural characterization of ZnO-doped MgO nanocomposites synthesized via sol–gel technique, BioNanoScience (2024) 1–14.

[14] K.S. Al-Namshah, M. Shkir, F.A. Ibrahim, M.S. Hamdy, Auto combustion synthesis and characterization of Co doped ZnO nanoparticles with boosted photocatalytic performance, Phys. B: Condens. Matter 625 (2022) 413459.

[15] M. Shkir, J. Hakami, M. Milon Hossain, N.S. Awwad, A. Khan, Excellent photo-detection properties of cerium doped ZnO device fabricated by spray pyrolysis technique, Inorg. Chem. Commun. 140 (2022) 109439.

[16] A. Nebatti Ech Chergui, C. Pflitsch, B. Atakan, Atmospheric pressure metal-organic chemical vapor deposition (AP-MOCVD) growth of undoped and aluminium-doped ZnO thin film using hot wall reactor, Surf. Interfaces 22 (2021) 100883.

[17] X. Tian, H. Wu, X. Hu, Z. Wang, C. Ren, Z. Cheng, L. Dou, Y.-W. Lin, Enhanced photocatalytic performance of ZnO/AgCl composites prepared by high-energy mechanical ball milling, New J. Chem. 46 (2022) 9155–9171.

[18] R. Saad, A.M. Ahmed, K. Abdelkarem, M. Zayed, Z.M. Faidey, G.M. Al-Senani, M. Shaban, M.T. Tammam, H. Hamdy, SILAR-deposited CuO nanostructured films doped with zinc and sodium for improved CO2 gas detection, Nanomaterials 13 (2023) 2793.

[19] H. Safdar, R. Aydın, B. Şahin, Syntheses, structural evolution, electrical and optoelectronic characterization of ZnO/CuO composite films doped with transition metal $Mn^{2+}$ ions, Ceram. Int. 48 (2022) 26678–26688.

[20] S. Khurshid, H. Latif, Enhancement in absorption spectrum by ITO coated, down converting glass and increasing the SILAR cycles of PbS/CdS quantum dots sensitized ZnO nano with deposition of MoO3/Au/MoO3 (MAM) as a solid state solar cell, Opt. Mater. 142 (2023) 113915.

[21] M. Mohd Yusoff, A. Mahyuddin, Z. Hassan, M. Yahya, Effect of thermal annealing on ZnO/AlN/GaN/AlN heterostructure grown on Si substrate by radio frequency sputtering, Appl. Phys. A 129 (2023) 368.

[22] A. Muhammed, T.G. Asere, T.F. Diriba, Photocatalytic and antimicrobial properties of ZnO and Mg-doped ZnO nanoparticles synthesized using Lupinus albus leaf extract, ACS Omega 9 (2024) 2480–2490.

[23] G. Hosseinzadeh, S. Zinatloo-Ajabshir, A. Yousefi, Innovative synthesis of a novel ZnO/ZnBi2O4/graphene ternary heterojunction nanocomposite photocatalyst in the presence of tragacanth mucilage as natural surfactant, Ceram. Int. 48 (2022) 6078–6086.

[24] Mt.M. Alsmadi, N.K. Al-Nemrawi, R. Obaidat, A.E. Abu Alkahsi, K.M. Korshed, I. K. Lahlouh, Insights into the mapping of green synthesis conditions for Zno nanoparticles and their toxicokinetics, Nanomedicine 17 (2022) 1281–1303.

[25] J.J. Ahire, L.M. Dicks, Antimicrobial hyaluronic acid–cefoxitin sodium thin films produced by electrospraying, Curr. Microbiol. 73 (2016) 236–241.

[26] S. Withanage, A. Savin, V. Nikolaeva, A. Kiseleva, M. Dukhinova, P. Krivoshapkin, E. Krivoshapkina, Native spider silk-based antimicrobial hydrogels for biomedical applications, Polymers (2021).

[27] M.M. Pérez-Madrigal, J.E. Shaw, M.C. Arno, J.A. Hoyland, S.M. Richardson, A. P. Dove, Robust alginate/hyaluronic acid thiol–yne click-hydrogel scaffolds with superior mechanical performance and stability for load-bearing soft tissue engineering, Biomater. Sci. 8 (2020) 405–412.

[28] A. Abbas, T. Ahmad, S. Hussain, M. Noman, T. Shahzad, A. Iftikhar, Cheema, M. Ijaz, M. Tahir, G. Gohari, Immobilized biogenic zinc oxide nanoparticles as photocatalysts for degradation of methylene blue dye and treatment of textile effluents, Int. J. Environ. Sci. Technol. 19 (2022) 11333–11346.

[29] M. Aghazadeh, A.H. Hassani, M. Borghei, Application of photocatalytic proxone process for petrochemical wastewater treatment, Sci. Rep. 13 (2023) 12738.

[30] S. Khan, T. Noor, N. Iqbal, L. Yaqoob, Photocatalytic dye degradation from textile wastewater: a review, ACS Omega 9 (2024) 21751–21767.

[31] S. Yasmeen, L. Burratti, L. Duranti, E. Sgreccia, P. Prosposito, Photocatalytic degradation of organic pollutants-nile blue, methylene blue, and bentazon herbicide-using NiO-ZnO nanocomposite, Nanomaterials 14 (2024).

[32] T. Wang, I. Hussain, L. Ma, Y. Zhong, W. Zhang, G. Yang, Rational synthesis of two isostructural thiophene-containing metal-organic frameworks toward photocatalytic degradation of organic pollutants, J. Colloid Interface Sci. 660 (2024) 681–691.

[33] M.D. Yilmaz, N.G. Ozsamur, S. Erbas-Cakmak, Catalytic investigation of hyaluronic acid-stabilized Ag nanoparticles as non-toxic nanocatalysts in the oxidation of morin, New J. Chem. 48 (2024) 2341–2347.

[34] O. Kahveci, A. Akkaya, E.K. Sarıkaya, M. Çanlı, R. Aydın, B. Şahin, E. Ayyıldız, Construction of unary and ternary ZnO–CuO–CdO composite thin films and comprehensive analysis of their optical, electrical, and photocatalytic performance, J. Alloy. Compd. 997 (2024) 174827.

[35] R. Aydın, B. Şahin, The role of Triton X-100 as a surfactant on the CdO nanostructures grown by the SILAR method, J. Alloy. Compd. 705 (2017) 9–13.

[36] A. Akkaya, E. Ayyıldız, Automation software for semiconductor research laboratories: electrical parameter calculation program (SeCLaS-PC), J. Circuits Syst. Comput. 29 (2020) 2050215.

[37] A. Akkaya, E. Ayyıldız, Automation software for semiconductor research laboratories: measurement system and instrument control program (SeCLaS-IC), MAPAN 35 (2020) 343–350.

[38] Y. Zhang, Q. Wang, J. Xu, S. Ma, Synthesis of Pd/ZnO nanocomposites with high photocatalytic performance by a solvothermal method, Appl. Surf. Sci. 258 (2012) 10104–10109.

[39] S. Harish, J. Archana, M. Sabarinathan, M. Navaneethan, K.D. Nisha, S. Ponnusamy, C. Muthamizhchelvan, H. Ikeda, D.K. Aswal, Y. Hayakawa, Controlled structural and compositional characteristic of visible light active ZnO/CuO photocatalyst for the degradation of organic pollutant, Appl. Surf. Sci. 418 (2017) 103–112.

[40] M.N. Chong, B. Jin, C.W.K. Chow, C. Saint, Recent developments in photocatalytic water treatment technology: a review, Water Res. 44 (2010) 2997–3027.

[41] R. Al-Khateeb, J. Prpic, M. Eliezer, Hyaluronic acid unique identification prints in perspective of its 3D microscop-ical structure as a carbohydrate hydrogel with various phys-iochemical and biological functions, Arch. Oral Maxillofac. Surg. 4 (2021) 105–117.

[42] S. Chen, Q. Zhang, T. Nakamoto, N. Kawazoe, G. Chen, Highly active porous scaffolds of collagen and hyaluronic acid prepared by suppression of polyion complex formation, J. Mater. Chem. B 2 (2014) 5612–5619.

[43] F. Mohammadi, S.M. Samani, N. Tanideh, F. Ahmadi, Hybrid scaffolds of hyaluronic acid and collagen loaded with prednisolone: an interesting system for osteoarthritis, Adv. Pharm. Bull. 8 (2018) 11.

[44] S. Chen, Q. Zhang, N. Kawazoe, G. Chen, Effect of high molecular weight hyaluronic acid on chondrocytes cultured in collagen/hyaluronic acid porous scaffolds, Rsc Adv. 5 (2015) 94405–94410.

[45] B. Perk, Y.T. Büyüksünetçi, Ü. Anık, Gold nanoparticle deposited electrochemical sensor for hyaluronic acid detection, Chem. Pap. 77 (2023) 4319–4329.

[46] M.S. Bae, D.H. Yang, J.B. Lee, D.N. Heo, Y.-D. Kwon, I.C. Youn, K. Choi, J. H. Hong, G.T. Kim, Y.S. Choi, E.H. Hwang, I.K. Kwon, Photo-cured hyaluronic acid-based hydrogels containing simvastatin as a bone tissue regeneration scaffold, Biomaterials 32 (2011) 8161–8171.

[47] S. Wang, S. Guan, Z. Zhu, W. Li, T. Liu, X. Ma, Hyaluronic acid doped-poly(3,4-ethylenedioxythiophene)/chitosan/gelatin (PEDOT-HA/Cs/Gel) porous conductive scaffold for nerve regeneration, Mater. Sci. Eng.: C 71 (2017) 308–316.

[48] Ş.T. Okulmuş, B. Oktay, D. Kazan, N.K. Apohan, Development of bacterial cellulose-hyaluronic acid multicomponent hydrogels via click chemistry for biomedical applications, Polym. Sci. Ser. A 65 (2023) 682–691.

[49] J.-H. Choi, S.-O. Kim, E. Linardy, E.C. Dreaden, V.P. Zhdanov, P.T. Hammond, N.-J. Cho, Adsorption of hyaluronic acid on solid supports: role of pH and surface chemistry in thin film self-assembly, J. Colloid Interface Sci. 448 (2015) 197–207.

[50] K.A. Wygladacz, D.J. Hook, Visualization of a hyaluronan network on the surface of silicone-hydrogel materials, Clin. Ophthalmol. 10 (2016) 1423–1433.

[51] K. Lewandowska, A. Sionkowska, M. Kurzawa, Physical properties and release profiles of chitosan mixture films containing salicin, glycerin and hyaluronic acid, Molecules 28 (2023).

[52] G.K. Mani, J.B.B. Rayappan, Influence of copper doping on structural, optical and sensing properties of spray deposited zinc oxide thin films, J. Alloy. Compd. 582 (2014) 414–419.

[53] O. Kahveci, A. Akkaya, R. Aydın, B. Şahin, E. Ayyıldız, Synthesis of Al and In dual-doped CuO nanostructures via SILAR method: structural, optical and electrical properties, Inorg. Chem. Commun. 147 (2023) 110230.

[54] S. Pat, R. Mohammadigharehbagh, S. Özen, V. Şenay, H.H. Yudar, Ş. Korkmaz, The Al doping effect on the surface, optical, electrical and nanomechanical properties of the ZnO and AZO thin films prepared by RF sputtering technique, Vacuum 141 (2017) 210–215.

[55] P. Scherrer, Bestimmung der Grösse und der inneren von Kolloidteilchen mittels Röntgenstrahlen Struktur Nachr, Ges. Wiss. Göttingen 26 (1918) 98–100.

[56] E. Asfuroğlu Coşkun, B. Şahin, Mg-substituted ZnO/CuO composite films: a potential candidate for highly efficient human hydration level monitoring, Sens. Actuators A: Phys. 328 (2021) 112770.

[57] Y. Abdollahi, A. Abdullah, Z. Zainal, N. Yusof, Synthesis and characterization of manganese doped ZnO nanoparticles, Int. J. Basic Appl. Sci. 11 (2011) 62–69.

[58] U. Pal, C.W. Kim, N.A. Jadhav, Y.S. Kang, Ultrasound-assisted synthesis of mesoporous ZnO nanostructures of different porosities, J. Phys. Chem. C 113 (2009) 14676–14680.

[59] C. Chen, P. Liu, C. Lu, Synthesis and characterization of nano-sized ZnO powders by direct precipitation method, Chem. Eng. J. 144 (2008) 509–513.

[60] D. Raoufi, Synthesis and microstructural properties of ZnO nanoparticles prepared by precipitation method, Renew. Energ. 50 (2013) 932–937.

[61] M. Messali, F. Al Wadaani, H. Oudghiri-Hassani, S. Rakass, S. Al Amri, M. Benaissa, M. Abboudi, Preparation, characterization and photocatalytic activity of hexagonal ZnO nanoparticles, Mater. Lett. 128 (2014) 187–190.

[62] A.M. Hussein, L. Mahoney, R. Peng, H. Kibombo, C.-M. Wu, R.T. Koodali, R. Shende, Mesoporous coupled ZnO/$TiO_2$ photocatalyst nanocomposites for hydrogen generation, J. Renew. Sustain. Energy 5 (2013).

[63] X. He, Y. Yang, Y. Li, J. Chen, S. Yang, R. Liu, Z. Xu, Effects of structure and surface properties on the performance of ZnO towards photocatalytic degradation of methylene blue, Appl. Surf. Sci. 599 (2022) 153898.

[64] K. Ogorzały, G. Jajko, A. Korzeniowska, M. Mazur, A. Li, W.J. Roth, B. Gil, W. Makowski, The effect of amorphous silica support on the catalytic activity of liquid-exfoliated monolayered MCM-56 zeolite, J. Porous Mat. 30 (2023) 1459–1468.

[65] J. Jagiello, J. Kenvin, NLDFT adsorption models for zeolite porosity analysis with particular focus on ultra-microporous zeolites using $O_2$ and $H_2$, J Colloid Interface Sci. 625 (2022) 178–186.

[66] M. Bulla, V. Kumar, R. Devi, S. Kumar, A.K. Sisodiya, R. Dahiya, A.K. Mishra, Natural resource-derived NiO nanoparticles via Aloe vera for high-performance symmetric supercapacitor, Sci. Rep. 14 (2024) 7389.

[67] S. Soğan, E. Yücel, E.K. Sarıkaya, O. Kahveci, R. Aydın, A. Akkaya, B. Şahin, Growth and characterization of Fe-doped CuO/ZnO binary oxide thin films for possible optoelectronic applications, Opt. Mater. 152 (2024) 115557.

[68] M.I. Khan, J. Iqbal, S.J. Akram, Y.A. El-Badry, M. Yaseen, R.A. Khera, End-capped group modification on cyclopentadithiophene based non-fullerene small molecule acceptors for efficient organic solar cells; a DFT approach, J. Mol. Graph. Model. 113 (2022) 108162.

[69] Y.J. Kwon, C.S. Lim, K.B. Shim, Characterization of ZnO nanopowders synthesized by the polymerized complex method via an organochemical route, J. Ceram. Process. Res. 3 (2002) 146–149.

[70] R. Keuleers, H.O. Desseyn, B. Rousseau, C. Van, Alsenoy, Vibrational analysis of urea, J. Phys. Chem. A 103 (1999) 4621–4630.

[71] T. Munawar, F. Iqbal, S. Yasmeen, K. Mahmood, A. Hussain, Multi metal oxide NiO-CdO-ZnO nanocomposite–synthesis, structural, optical, electrical properties and enhanced sunlight driven photocatalytic activity, Ceram. Int. 46 (2020) 2421–2437.

[72] D. Raoufi, Synthesis and photoluminescence characterization of ZnO nanoparticles, J. Lumin. 134 (2013) 213–219.

[73] J.S. Reparaz, F. Güell, M.R. Wagner, A. Hoffmann, A. Cornet, J.R. Morante, Size-dependent recombination dynamics in ZnO nanowires, Appl. Phys. Lett. 96 (2010).

[74] I. Ahmad, E. Ahmed, M. Ahmad, The excellent photocatalytic performances of silver doped ZnO nanoparticles for hydrogen evolution, SN Appl. Sci. 1 (2019) 327.

[75] R.S. Sabry, W.J. Aziz, M.I. Rahmah, Employed silver doping to improved photocatalytic properties of ZnO micro/nanostructures, J. Inorg. Organomet. Polym. Mater. 30 (2020) 4533–4543.

[76] L.-W. Lai, C.-T. Lee, Investigation of optical and electrical properties of ZnO thin films, Mater. Chem. Phys. 110 (2008) 393–396.

[77] A.B. Djurišić, Y.H. Leung, Optical properties of ZnO nanostructures, Small 2 (2006) 944–961.

[78] S. Hong, T. Joo, W.I. Park, Y.H. Jun, G.-C. Yi, Time-resolved photoluminescence of the size-controlled ZnO nanorods, Appl. Phys. Lett. 83 (2003) 4157–4159.

[79] Z. Zaaboub, F. Hassen, L. Chaabane, H. Maaref, Photoluminescence and time resolved photoluminescence properties in as grown ZnO thin films prepared by DC reactive sputtering for optoelectronic devices, Microelectron. J. 114 (2021) 105153.

[80] Y. Li, H.-y Feng, N. Zhang, C.-s Liu, Solvo-thermal synthesis and characterization of nest-like zinc oxide, T Nonferrous Met. Soc. 20 (2010) 119–122.

[81] D.H. Zhang, Q.P. Wang, Z.Y. Xue, Photoluminescence of ZnO films excited with light of different wavelength, Appl. Surf. Sci. 207 (2003) 20–25.

[82] R. Raji, K.G. Gopchandran, ZnO nanostructures with tunable visible luminescence: effects of kinetics of chemical reduction and annealing, J. Sci.: Adv. Mater. Devices 2 (2017) 51–58.

[83] J.K. Tsai, J.H. Shih, T.C. Wu, T.H. Meen, n-ZnO nanorods/$p^+$-Si (111) heterojunction light emitting diodes, Nanoscale Res. Lett. 7 (2012) 664.

[84] S.A. Studenikin, N. Golego, M. Cocivera, Fabrication of green and orange photoluminescent, undoped ZnO films using spray pyrolysis, J. Appl. Phys. 84 (1998) 2287–2294.

[85] D.K. Schroder, Semiconductor Material And Device Characterization, John Wiley & Sons, New York, 2006.

[86] A. Akkaya, O. Kahveci, B. Şahin, E. Ayyıldız, Simultaneously-doping of $HfO_2$ thin films by Ni with sputtering technique and effect of post annealing on structural and electrical properties, Phys. B: Condens. Matter 665 (2023) 415034.

[87] A. Asadov, W. Gao, Z. Li, J. Lee, M. Hodgson, Correlation between structural and electrical properties of ZnO thin films, Thin Solid Films 476 (2005) 201–205.

[88] J. Liu, Y. Wang, J. Ma, Y. Peng, A. Wang, A review on bidirectional analogies between the photocatalysis and antibacterial properties of ZnO, J. Alloy. Compd. 783 (2019) 898–918.

[89] R.M. Hewlett, M.A. McLachlan, Surface structure modification of ZnO and the impact on electronic properties, Adv. Mater. 28 (2016) 3893–3921.

[90] B. Polyakov, A. Novikovs, M. Leimane, K. Kadiwala, M. Zubkins, E. Butanovs, S. Oras, E. Damerchi, V. Zadin, S. Vlassov, Comparison of the resistivities of nanostructured films made from silver, copper-silver and copper nanoparticle and nanowire suspensions, Thin Solid Films 784 (2023) 140087.

[91] S. Karim, W. Ensinger, T.W. Cornelius, R. Neumann, Investigation of size effects in the electrical resistivity of single electrochemically fabricated gold nanowires, Phys. E: Low-Dimens. Syst. Nanostruct. 40 (2008) 3173–3178.

[92] B. Şahin, M. Alomari, T. Kaya, Hydration detection through use of artificial sweat in doped- and partially-doped nanostructured CuO films, Ceram. Int. 41 (2015) 8002–8007.

[93] S. Sreehari, N.S. George, L.M. Jose, S. Nandakumar, R.T. Subramaniam, A. Aravind, A review on 2D transition metal nitrides: structural and morphological impacts on energy storage and photocatalytic applications, J. Alloy. Compd. 950 (2023) 169888.

[94] V.H. Nguyen, D.V.N. Vo, S. Nanda, Nanostructured photocatalysts: from fundamental to practical applications, Elsevier Sci. (2021).

[95] J.C. Colmenares, R. Luque, J.M. Campelo, F. Colmenares, Z. Karpiński, A. A. Romero, Nanostructured photocatalysts and their applications in the photocatalytic transformation of lignocellulosic biomass: an overview, Materials 2 (2009) 2228–2258.

[96] P.K. Sahu, A. Champati, A. Pradhan, B. Naik, Design and development of nanostructured photocatalysts for large-scale solar green hydrogen generation, Sustain. Energy Fuels 8 (2024) 1872–1917.

[97] M. Kojima, T. Takagi, C. Matsubara, K. Nakamura, Methylene blue sensitized degradation of sodium hyaluronate through photoinduced electron transfer, Chem. Lett. 29 (2000) 354–355.

[98] D. Pasqui, A. Atrei, R. Barbucci, The immobilization of titania nanoparticles on hyaluronan films and their photocatalytic properties, Nanotechnology 20 (2009) 015703.

[99] H.A. Kiwaan, T.M. Atwee, E.A. Azab, A.A. El-Bindary, Photocatalytic degradation of organic dyes in the presence of nanostructured titanium dioxide, J. Mol. Struct. 1200 (2020) 127115.

[100] A. Nisar, M. Saeed, M. Muneer, M. Usman, I. Khan, Synthesis and characterization of ZnO decorated reduced graphene oxide (ZnO-rGO) and evaluation of its photocatalytic activity toward photodegradation of methylene blue, Environ. Sci. Pollut. Res. 29 (2022) 418–430.

[101] H.F. Greer, W. Zhou, G. Zhang, H. Ménard, Nanocone decorated ZnO microspheres exposing the (0001) plane and enhanced photocatalytic properties, Adv. Mater. Interfaces 4 (2017) 1601238.

[102] W. Kang, X. Jimeng, W. Xitao, The effects of ZnO morphology on photocatalytic efficiency of ZnO/RGO nanocomposites, Appl. Surf. Sci. 360 (2016) 270–275.

[103] H. Tong, S. Ouyang, Y. Bi, N. Umezawa, M. Oshikiri, J. Ye, Nano-photocatalytic materials: possibilities and challenges, Adv. Mater. 24 (2012) 229–251.

[104] S. Goktas, A. Goktas, A comparative study on recent progress in efficient ZnO based nanocomposite and heterojunction photocatalysts: a review, J. Alloy. Compd. 863 (2021) 158734.
[105] M. Dovedytis, Z.J. Liu, S. Bartlett, Hyaluronic acid and its biomedical applications: a review, Eng. Regen. 1 (2020) 102–113.
[106] S. Kozuch, J.M.L. Martin, "Turning over" definitions in catalytic cycles, Acs Catal. 2 (2012) 2787–2794.
[107] L. Gomathi Devi, R. Shyamala, Photocatalytic activity of $SnO_2$–α-$Fe_2O_3$ composite mixtures: exploration of number of active sites, turnover number and turnover frequency, Mater. Chem. Front. 2 (2018) 796–806.
[108] C.-L. Chiang, K.-S. Lin, H.-W. Chuang, Direct synthesis of formic acid via $CO_2$ hydrogenation over Cu/ZnO/$Al_2O_3$ catalyst, J. Clean. Prod. 172 (2018) 1957–1977.
[109] D.S. Bhattacharya, D. Svechkarev, J.J. Souchek, T.K. Hill, M.A. Taylor, A. Natarajan, A.M. Mohs, Impact of structurally modifying hyaluronic acid on CD44 interaction, J. Mater. Chem. B 5 (2017) 8183–8192.
[110] R. Peach, D. Hollenbaugh, I. Stamenkovic, A. Aruffo, Identification of hyaluronic acid binding sites in the extracellular domain of CD44, J. Cell Biol. 122 (1993) 257–264.